ROYAL SOCIETY
OF CHEMISTRY

COMMUNICATION

Check for updates

The sensitivity of Cu for electrochemical carbon dioxide reduction to hydrocarbons as revealed by high throughput experiments†

Yungchieh Lai, [ID] [a] Ryan J. R. Jones, [ID] [a] Yu Wang, [ID] [a] Lan Zhou, [ID] [a] Matthias H. Richter [ID] [a] and John Gregoire [ID] ⋆[ab]

Electrochemical CO_2 reduction to valuable products is a centerpiece of future energy technologies that relies on identification of new catalysts. We present accelerated screening of Cu bimetallic alloys, revealing remarkable sensitivity to alloy concentration that indicates the migration of alloying elements to critical sites for hydrocarbon formation.

The promise of electrochemical CO_2 reduction to valuable products has prompted substantial research in selective catalysis of the many-electron reduction of CO_2 to products such as light hydrocarbons.[1] However, most metal electrocatalysts have been shown to exclusively form the 2 e⁻ products CO and formate (*e.g.* Au, Ag, In, and Sn) and/or catalyze the competing hydrogen evolution reaction (HER) (*e.g.* Fe, Ni, Pt, and Ti).[2] Cu is the only known elemental catalyst capable of reducing CO_2 to hydrocarbons (HCs) and alcohols with appreciable faradaic efficiency (FE) but suffers from poor selectivity to any single product and high overpotentials for generating the highly reduced products.[2–4] The uniqueness of Cu has been understood to be due to its moderate binding energy of CO and other intermediates.[5,6] Alloying with a secondary metal is a widely-adopted strategy to alter a catalyst's adsorption energetics for reactants and intermediates, and some copper-based bimetallic catalysts have been evaluated for altering the CO_2RR selectivity.[7] While improved selectivity for 2 e⁻ products has been achieved, success in increasing FE for higher order products has been more limited, as discussed further below.[8–22] Comparison among reported Cu-alloy systems is limited by the variation in catalyst syntheses and morphologies in these studies, motivating the systematic study of different alloying elements and alloying concentrations in the present work.

Exploration of CO_2RR electrocatalysts is hampered by the dearth of accelerated screening systems, which are challenging to realize given the sensitivity of product distribution to the electrochemical environment and the breadth of possible reaction products. The ideal characterization of a given catalyst is quantitative measurement of the activity and product distribution, as a function of time and for a large range of overpotentials since product distributions vary with aging of the operational catalyst as well as the operating potential. This combination of desired measurement attributes is incompatible with traditional methods,[3] perhaps most notably due to the duration of quantitative product distribution measurements *via* chromatography or nuclear magnetic resonance, which severely limits the measurement frequency to observe variations in product distribution as a function of time and/or overpotential.

Electrochemical reactor with online mass spectroscopy to detect reaction products has been developed in experimental techniques such as differential electrochemical mass spectrometry (DEMS)[23–25] and has recently has deployed for "real-time" CO_2RR product detection with scanning electrochemical cells.[22,26,27] Clark *et al.*[24,28] introduced a modified traditional/dual thin-layer DEMS flow cell that provides excellent characterization of individual CO_2RR electrocatalysts with quantified product. We combine the scanning cell concept for combinatorial measurements with a DEMS-style product detection system that is decoupled from the electrochemical cell to mitigate interference of product detection in the electrochemical reactor. By additionally introducing selective differential pumping of water vapor in vacuum, we demonstrate quantitative faradaic efficiency (FE) measurement of H_2, CH_4, and C_2H_4 during cyclic voltammetry (CV) experiments with a measurement interval of 12 s, enabling rapid screening of arrays of catalyst compositions.

Through exploration of the ASM binary alloy phase diagrams[29] we identified 8 non-precious metals that alloy into fcc-Cu by at least 10 at% for some temperature below 700 °C. Binary compositionally-graded thin films of each Cu–X system with compositions range from below 3 at% to above 18 at% of

[a]Joint Center for Artificial Photosynthesis, California Institute of Technology, Pasadena, CA 91125, USA. E-mail: gregoire@caltech.edu

[b]Division of Engineering and Applied Science, California Institute of Technology, Pasadena, CA 91125, USA

† Electronic supplementary information (ESI) available: Additional experimental description and alternate visualizations of data. See DOI: 10.1039/c9ta10111j

the alloying element were prepared by combinatorial sputtering and measured at 8 alloy compositions, creating a library of 64 alloys (Table S1†) that were each evaluated by a series of 3 CVs using the instrument shown in Fig. 1. The electrolyte flow at 0.16 mL s^{-1} through a catholyte chamber of *ca.* 0.32 mL creates a liquid-only electrochemical reactor except during sustained production of products beyond their solubility limit, *e.g.* prolonged partial current density above *ca.* 5 mA cm^{-2} for gaseous products. The electrolysis effluent flows through a pervaporator cell with poly(tetrafluoroethylene) (PTFE) membrane, where the vacuum contact promotes evaporation of volatile dissolved species such as H_2, CH_4, and C_2H_4. The concomitant evaporation of water requires substantial differential pumping, traditionally by a mechanical pump that also discards the vast majority of the reaction products. This issue is circumvented in the present work with an in-line molecular sieve (mol. sieve) desiccant chamber that sorbs water and alcohols to increase the partial pressure of HCs in the MS inlet by a factor of approximately 100 (Fig. S2†).[31] As a result, with 12 s MS measurement intervals, HCs can be detected at partial current densities (J_p) above 30 μA cm^{-2}. The MS signals at mass-to-charge (*m/z*) values of 2, 15, and 26 provide quantitative measurement of the partial pressure of H_2, CH_4, and C_2H_4 in the post-desiccant vacuum effluent, whose signals are calibrated by saturating the flowing electrolyte with calibration gases with the cell held at open circuit. While other strategies for online product detection have enabled accelerated screening of electrocatalysts,[22,28,30,32] we note a unique aspect of the present work is that the rapid flow and decoupling of the reactor and pervaporator ensure that products created from the entire working electrode are detected, as opposed to localized product extraction where spatial variations in mass transport, *etc.* can cause the measured product stream to poorly represent the electrochemical measurement, creating artifacts in the inferred FE, *etc.*

Given the excellent partial current density detectability limit, the MS signals can be directly used for identifying catalysts and electrolysis settings that yield HCs. For the present purposes of identifying whether Cu alloys alter FE for HCs, especially at lower overpotentials, a CV is the desired electrochemical technique, but appreciable potential scanning rates and/or potential-dependent partial current densities result in the inability of the MS signal to reach steady state. We established a model for calculating the time-dependent partial current density of each product from the respective measured time-dependent MS signal, as described previously.[31] For CVs at 10 mV s^{-1} between un-compensated potentials of −0.4 and −1.3 V *vs.* RHE, we find that J_p is well modelled by assuming that J_p is the same function of applied potential during both the cathodic and anodic voltage sweeps. Furthermore, this function can be approximated by a Gaussian, which represents a peak in J_p when the center potential of the Gaussian is within the CV limits and could also approximate an exponential function when the center potential is beyond the CV limits. Consequently, the series of MS measurements per product and per CV cycle are used to determine the corresponding 3 Gaussian parameters that minimize the loss between the modelled and measured MS signal. Fig. S3–S5† shows the stability of the measurement and of this J_p modelling algorithm through repeated measurements on a series of Cu thin film catalysts. The product selectivity and partial current shown agrees well with those of polycrystalline Cu reported in the literature.[3,30] Fig. 2a illustrates the measurement of 3 MS channels and working electrode current density over 3 CV cycles with
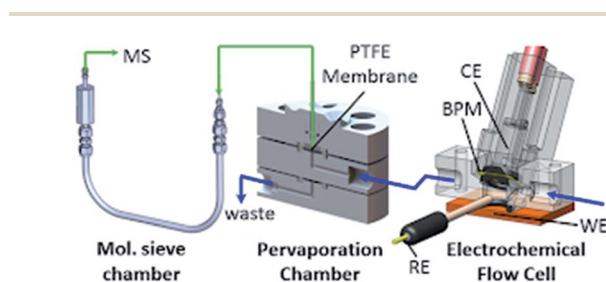
Fig. 1 Electrolyte (blue) and in-vacuum product stream (green) flows through the 3 components between the electrolyte reservoir and MS detector. The planar working electrode is pressed against the o-ring at the bottom of the electrochemical cell. The inlet flow tube is directed toward the working electrode (WE), and the outlet flow tube terminates near the membrane at the top of the cell so that any bubbles are readily removed. The reference electrode (RE) is horizontal, terminating near the center of the chamber, *ca.* 2.8 mm above the WE, and the counter electrode (CE) is separated by the bipolar membrane (BPM). The electrolyte is then injected in the center of a cylindrical pervaporation chamber with volatile species crossing the PTFE membrane, creating a product stream that is differentially pumped by the mol. sieve before continuous injection in the MS for product quantification.
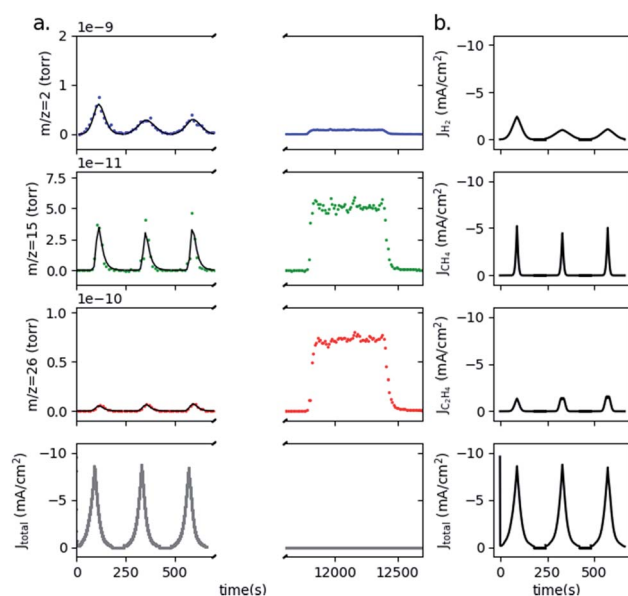
Fig. 2 EC-MS demonstration with a thin film Cu electrode. (a) Typical experimental process for catalyst screening including 3 CV cycles separated by OCP for enabling MS to return to baseline. After performing such measurements on a series of catalysts, a daily calibration is performed by flowing through electrolyte bubbled with calibration gas containing 0.4% H_2, 0.4% CH_4, and 0.4% C_2H_4 in CO_2. (b) Using this calibration and pervaporation model, the modeled partial current density for each species is calculated and compared to the measured total current.

60 s of open circuit potentiometry (OCP) in between to allow MS signals to return to baseline so that each CV can be modelled independently. Fig. 2b shows the J_p resulting from the 3-parameter Gaussian fit using a custom fitting procedure described previously.[31] The MS signal corresponding to this fit is also shown in Fig. 2a. It is worth noting that the resulting J_p is quite similar on the second and third cycles, which can differ from that of the first cycle. This variability in the first CV is expected since no electrochemical pretreatment was performed on the sputtered film and is likely related to contaminants and/or oxidation from air exposure. As a result, the evolving product distribution during the first cycle exceeds the scope of the Gaussian-based model described above and corresponds to substantial uncertainty in the precise shape of J_p in Fig. 2b. While additional modelling can be used to explore this first cycle, for the purposes of the present work we note that for all alloy catalysts the results of the second and third cycle are consistent, motivating our analysis and reporting of only the third cycle. The measured current is also smoothed with a 129-point cubic Savitzky–Golay filter and then compensated for resistive losses using the measured 60 Ω cell resistance. Uncompensated versions of each such figure are included in the ESI.†

Fig. 3 shows the MS measurements and subsequent modelling for the 8 alloy composition systems along with that of a pure Cu reference. Catalysts exhibiting current densities in excess of 5 mA cm^{-2} for a substantial fraction of each CV cycle typically causing bubble formation that gives rise to the large positive outlier values in the MS measurements. While such data points cause some uncertainty in the resulting J_p, the modelling procedure mitigates sensitivity to the outlier and preferably weights the data points at the onset of product detection.[31]

Complete datasets for 8 alloy systems elements are provided as Fig. S6–S13,† and 3 includes the compilation of the $Cu_{0.95}X_{0.05}$ compositions. A range of potential-dependent FE signals for each product are observed, and the observed

differences from the Cu-only catalyst are quite remarkable. The figure also indicates substantial variation in the total current density, which is shown for these compositions in Fig. 4a. To further probe the composition-dependent product distributions, we consider the integral over time of this total current density as well as over each product-specific J_p, yielding electrolysis charge densities for the entire CV. The results shown in Fig. 4b include a dashed line indicating the average over the Cu measurements in Fig. S4.†

To unpack this wealth of data we consider alloying elements that behave qualitatively similar and discuss in the context on the Cu alloy literature, which mostly involves higher concentrations of the alloying element. The lack of literature on dilute alloys of fcc-Cu is emblematic of the intuition that small concentrations of alloying elements will have no substantial impact on the catalysis, yet Fig. 4b shows that 2–3 at% of Sb, In or Sn is sufficient to lower total HC production during the CV by a factor of 10 or more, a level of sensitivity to an alloying element that to our knowledge has no precedent in electrocatalysis when the contaminant is an alloying element that is itself an electrocatalyst, as opposed to contaminants such as S and Cl that readily poison metal surfaces.[33,34] It is worth noting
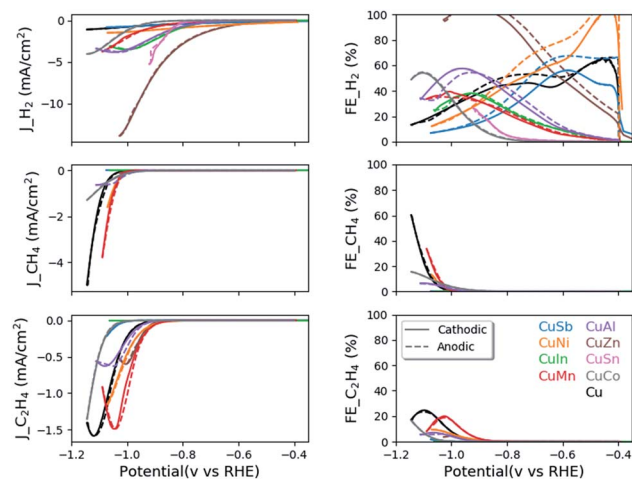

Fig. 4 For each of 8 alloy elements, the (a) total current density and (b) charge density (integral of J_p over time(s)) for the third CV cycle is shown as a function of alloy concentration. The dashed black line indicates the average charge density for pure Cu. The bottom 3 panels include a broken charge density axis corresponding to product generation near or below the detectability limit.

Fig. 3 The J_p (left column) and FE (right column) for the third CV cycle is shown for each of the 8 Cu-based bimetallic catalysts with *ca.* 5% of the alloying metal. The potentials include resistance compensation and legends in bottom-right panel apply to all 6 panels.
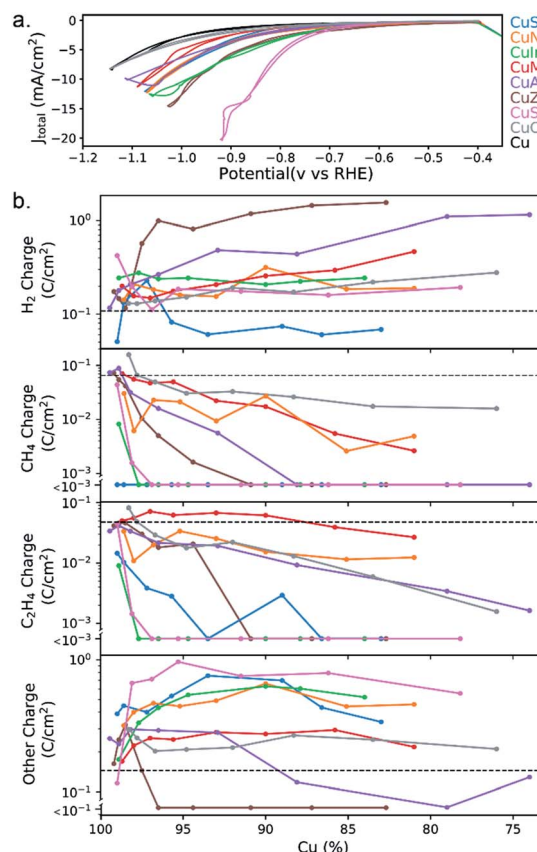
This journal is © The Royal Society of Chemistry 2019

J. Mater. Chem. A, 2019, **7**, 26785–26790 | **26787**

that in the CV experiments, high partial current density for non-HC products mitigates the ability to form HCs, not only due to the competitive concentrations of reaction intermediates, but also due to resistive losses as reflected in the range of applied potentials after resistance compensation shown in Fig. 4a.

Sb, In, and Sn alloys exhibit a substantial increase in the current density with the FE for H_2 being relatively unchanged, indicating that the suppression in HC formation is commensurate with a substantially increased activity for other products, which were confirmed to be 2 e^- products CO and formate *via* detailed experiments on select catalysts (see ESI†). These results are in agreement with previous reports on Cu–In[9–11] and Cu–Sn[14] catalysts where the weak H adsorption and strong O binding of In and Sn enhances selectivity toward formate and CO. For example, FE of 90% for formate with Cu–Sn and for CO with Cu–In were reported at low potentials, with the present work being the first to explore more dilute alloys of these elements. While further study of the highly active Cu–(Sb, In, Sn) catalysts may be of interest for formation of products other than HCs, their primary scientific importance for CO_2RR is understanding how such a small concentration can so strongly influence product distribution, with Cu–Sb affecting CH_4 and C_2H_4 differently (see below). In the concerted community effort to understand the uniqueness of Cu, these alloys provide a new line of inquiry.

The Cu–Zn alloys share some important similarities and differences compared to the Sb, In, and Sn systems. The HC formation is less sensitive to alloy concentration in the 2–6 at% range. Catalysts with higher Zn concentrations exhibit the highest H_2 production among all the alloys, which not only hampers formation of HCs but also other CO_2RR products. These results are somewhat surprising given literature precedent of Cu–Zn catalysts. Zn-rich alloy films[35] and nanoporous Zn-rich structures[18] have been studied for formate and CO production at low overpotential, which are not directly comparable to the Zn-poor catalysts in Fig. 4 and collectively indicate that product distributions of Cu–Zn catalysts do not vary monotonically with composition. Zn coatings on Cu have been shown to suppress HER and increase CH_4 production,[36] in stark contrast to the results of Fig. 4, indicating that the surface and near-surface Zn in the alloy catalysts of the present work are critically different from the previously reported application of Zn coatings. Ren *et al.*[37] studied electrodeposited Cu–Zn alloys with Zn concentrations of 9–30 at% and focused on the increased ethanol production at high Zn concentrations. They also observed increased total current with Cu–Zn alloys compared to Cu at potentials above −0.95 V *vs.* RHE, in agreement with the present work, although the most Cu-rich alloy in that work (9 at% Zn) exhibited an increase in FE of C_2H_5OH, which is not measured by our study. Feng *et al.*[17] observed enhanced FE for C_2H_4 on oxide-derived Cu–Zn nanoparticles where Zn concentrations from 12 to 50 at% were studied, resulting in identification of 20 at% Zn as optimal for C_2H_4 formation. In this context, the results of Fig. 4 indicate that the morphology and exposed catalyst sites from the oxide-derived synthesis technique is more critical than the presence of Zn, which is commensurate with recent studies[38] on product-specific active sites in oxide-derived Cu catalysts and

motivates further inspection of whether Zn directly plays a catalytic role in increasing the FE of C_2H_4 or if it instead stabilizes the hypothesized unique Cu sites generated through electrochemical reduction from the metal oxide.[38]

While the 2 at% Co alloy enhances HC formation by a factor of about 2, Co is otherwise the most innocuous alloying element with no substantial change in the overall current and slightly increasing H_2 and decreasing HC production with increasing alloying concentration. Similar trends of HC formation over CuCo was observed by Grote and his coworkers where max production was found at Co concentration <10%.[22] Al is also somewhat innocuous with the primary effect being increase H_2 formation, which is markedly different from the heavier main group elements discussed above.

Other than the overall sensitivity of Cu to small alloying concentrations, perhaps the most intriguing observation is the select cases where the alloying element changes the relative production of CH_4 and C_2H_4, which is shown in Fig. S14.† The most Cu-rich alloys with Zn, Al, and Co slightly increase selectivity for CH_4. The 2–5 at% Sb catalysts are interesting in that they eliminate CH_4 from detectability but not C_2H_4, posing the possibility that improved catalysts could be obtained if this selectivity control could be harnessed without the increased FE in other products. This intriguing result was validated with more detailed experiments on the 2% Sb sample (see ESI†), which validated the observation of major CH_4 suppression with less C_2H_4 suppression and additionally revealed the CO is the primary contributor to the "Other charge" in Fig. 4. A similar but more gradual trend is observed with Mn (and to a lesser extent Ni) as relative C_2H_4 to CH_4 production increases with increasing alloy concentration, which was confirmed by additional experiments (see ESI†). While the total HC production of Ni also declines with increasing alloy concentration, the Mn alloys up to 5 at% show slightly higher total HC production, with the 3–4 at% Mn increasing the fraction of C_2 HCs (compared to total HCs) from the *ca.* 40 at% value observed with pure Cu to *ca.* 60 at%.

The alloys with 5 at% Cu–Sn and Cu–Mn were measured with XPS (Fig. S19†) to assess whether the near-surface concentrations of the alloying elements far exceeded the bulk values, and while enhancements of 1.6× and 2.8×, respectively, were observed, the sensitivity of product distribution to alloy concentration remains remarkable and largely unexplained by present understanding of CO_2RR on Cu-based catalysts. Theoretical characterization of absorption energies for bimetallic alloys[39] will help elucidate the composition-selectivity trends, although such data is not presently available in the dilute alloy concentration range and will additionally need to consider elemental surface segregation and reorganization processes. Since it is unlikely that such dilute alloys substantially alter the electronic structure of Cu, the most likely underlying phenomenon is that the HC-forming Cu sites have a relatively high surface energy that concomitantly drives surface alloying elements to these same sites, enabling a dilute concentration of these active sites to be contaminated by dilute alloy elements. Validating this hypothesis will require further experimentation and/or theoretical investigation, and the notable exceptions to

this trend, such as unique product distributions of Sb and Mn-based alloys, merit further investigation. The validation of the accelerated screening results with more detailed and traditional methods demonstrates the utility of the screening platform for catalyst discovery. These results also represent a cautionary tale for development of CO_2RR electrolysis devices as any plating of metal contaminants in the electrolyte can substantially alter product distributions, creating demanding requirements for elimination of trace metal contaminants. A notable precedence for this level of sensitivity to trace metals exists in alkaline oxygen evolution electrocatalysis where trace adventitious Fe from the electrolyte substantially influenced catalytic activity for initially Fe-free catalysts.[40] While the activity boost in that situation posed problems for scientific studies but not electrode development, the sensitivity of Cu to metal impurities poses more substantial challenges for electrocatalyst research and development.

Conclusions

We address challenges in CO_2 reduction electrocatalyst discovery through the design of an electrochemical flow cell with online mass spectroscopy-based quantification of the faradaic efficiency for H_2, CH_4, and C_2H_4 with 12 s measurement intervals and partial current detectability of *ca.* 0.03 mA cm^{-2}, enabling high throughput screening of Cu bimetallic alloys with Al, Mn, Co, Ni, Zn, In, Sn, and Sb. The product distribution of Cu-rich catalysts is remarkably sensitive to alloy concentration with 2 at% of some elements causing tenfold decrease of hydrocarbon formation, indicating that alloying elements segregate to critical sites for hydrocarbon formation, which poses substantial challenges for development and sustainable operation of Cu-based catalysts. Specific alloy concentrations of Sb and Mn increase C_2H_4 relative to CH_4, providing a new direction for catalyst development.

Conflicts of interest

There are no conflicts to declare.

Notes and references

1 P. D. Luna, C. Hahn, D. Higgins, S. A. Jaffer, T. F. Jaramillo and E. H. Sargent, *Science*, 2019, **364**, eaav3506.

2 Y. Hori, H. Wakebe, T. Tsukamoto and O. Koga, *Electrochim. Acta*, 1994, **39**, 1833–1839.

3 K. P. Kuhl, E. R. Cave, D. N. Abram and T. F. Jaramillo, *Energy Environ. Sci.*, 2012, **5**, 7050–7059.

4 S. Nitopi, E. Bertheussen, S. B. Scott, X. Liu, A. K. Engstfeld, S. Horch, B. Seger, I. E. L. Stephens, K. Chan, C. Hahn, J. K. Nørskov, T. F. Jaramillo and I. Chorkendorff, *Chem. Rev.*, 2019, **119**, 7610–7672.

5 K. P. Kuhl, T. Hatsukade, E. R. Cave, D. N. Abram, J. Kibsgaard and T. F. Jaramillo, *J. Am. Chem. Soc.*, 2014, **136**, 14107–14113.

6 A. A. Peterson and J. K. Nørskov, *J. Phys. Chem. Lett.*, 2012, **3**, 251–258.

7 A. Vasileff, C. Xu, Y. Jiao, Y. Zheng and S.-Z. Qiao, *Chem Rev.*, 2018, 1809–1831.

8 J. Christophe and T. Doneux, *Electrocatalysis*, 2012, **3**, 139–146.

9 A. Jedidi, S. Rasul, D. Masih, L. Cavallo and K. Takanabe, *J. Mater. Chem. A*, 2015, **3**, 19085–19092.

10 Z. B. Ho, T. S. Gray, K. B. Moraveck, T. B. Gunnoe and G. Zangari, *ACS Catal.*, 2017, **7**, 5381–5390.

11 G. O. Larrazábal, A. J. Martin, S. Mitchell, R. Hauert and J. Perez-Ramirez, *ACS Catal.*, 2016, 6265–6274.

12 S. Rasul, D. H. Anjum, A. Jedidi, Y. Minenkov, L. Cavallo and K. Takanabe, *Angew. Chem., Int. Ed.*, 2015, **54**, 2146–2150.

13 J. He, K. E. Dettelbach, D. A. Salvatore, T. Li and C. P. Berlinguette, *Angew. Chem., Int. Ed.*, 2017, **56**, 6068–6072.

14 M. Morimoto, Y. Takatsuji, R. Yamasaki, H. Hashimoto, I. Nakata, T. Sakakura and T. Haruyama, *Electrocatalysis*, 2018, **9**, 323–332.

15 M. Li, J. Wang, P. Li, K. Chang, C. Li, T. Wang and B. Jiang, *J. Mater. Chem. A*, 2016, **4**, 4776–4782.

16 D. Ren, B. S.-H. Ang and B. S. Yeo, *ACS Catal.*, 2016, **6**, 8239–8247.

17 Y. Feng, Z. Li, H. Liu, C. Dong, J. Wang, S. A. Kulinich and X. Du, *Langmuir*, 2018, **34**, 13544–13549.

18 H. Hu, Y. Tang, Q. Hu, P. Wan, L. Dai and X. J. Yang, *Appl. Surf. Sci.*, 2018, **445**, 281–286.

19 G. Yin, H. Abe, R. Kodiyath, S. Ueda, N. Srinivasan, A. Yamaguchi and M. Miyauchi, *J. Mater. Chem. A*, 2017, **5**, 12113–12119.

20 G. Keerthiga and R. Chetty, *J. Electrochem. Soc.*, 2017, **164**, H164–H169.

21 E. L. Clark, C. Hahn, T. F. Jaramillo and A. T. Bell, *J. Am. Chem. Soc.*, 2017, **139**, 15848–15857.

22 J. P. Grote, A. R. Zeradjanin, S. Cherevko, A. Savan, B. Breitbach, A. Ludwig and K. J. J. Mayrhofer, *J. Catal.*, 2016, **343**, 248–256.

23 H. Baltruschat, *J. Am. Soc. Mass Spectrom.*, 2004, **15**, 1693–1706.

24 E. L. Clark, M. R. Singh, Y. Kwon and A. T. Bell, *Anal. Chem.*, 2015, **87**, 8013–8020.

25 S. J. Ashton, *Design, construction and research application of a Differential Electrochemical Mass Spectrometer (DEMS)*, Springer Science & Business Media, 2012.

26 J. P. Grote, A. R. Zeradjanin, S. Cherevko and K. J. J. Mayrhofer, *Rev. Sci. Instrum.*, 2014, **85**, 104101.

27 P. Khanipour, M. Lçffler, A. M. Reichert, F. T. Haase, K. J. J. Mayrhofer and I. Katsounaros, *Angew. Chem., Int. Ed.*, 2019, **131**, 7273–7277.

28 E. L. Clark and A. T. Bell, *J. Am. Chem. Soc.*, 2018, **140**, 7012–7020.

29 *ASM Alloy Phase Diagram Database™ – ASM International*, https://www.asminternational.org/home/-/journal_content/56/10192/15469013/DATABASE, (accessed June 25, 2019).

30 E. L. Clark, M. R. Singh, Y. Kwon and A. T. Bell, *Anal. Chem.*, 2015, **87**, 8013–8020.

31 Y. Lai, R. J. R. Jones, Y. Wang, L. Zhou and J. M. Gregoire, *ACS Comb. Sci.*, 2019, **21**, 692–704.

This journal is © The Royal Society of Chemistry 2019

J. Mater. Chem. A, 2019, **7**, 26785–26790 | **26789**

32 K. Jambunathan, S. Jayaraman and A. C. Hillier, *Langmuir*, 2004, **20**, 1856–1863.

33 A. F. Ghenciu, *Curr. Opin. Solid State Mater. Sci.*, 2002, **6**, 389–399.

34 N. Job, M. Chatenet, S. Berthon-Fabry, S. Hermans and F. Maillard, *J. Power Sources*, 2013, **240**, 294–305.

35 G. Yin, H. Abe, R. Kodiyath, S. Ueda, N. Srinivasan, A. Yamaguchi and M. Miyauchi, *J. Mater. Chem. A*, 2017, **5**, 12113–12119.

36 G. Keerthiga and R. Chetty, *J. Electrochem. Soc.*, 2017, **164**, H164–H169.

37 D. Ren, B. S.-H. Ang and B. S. Yeo, *ACS Catal.*, 2016, **6**, 8239–8247.

38 Y. Lum and J. W. Ager, *Nat. Catal.*, 2019, **2**, 86.

39 O. Mamun, K. T. Winther, J. R. Boes and T. Bligaard, *Sci. Data*, 2019, **6**, 76.

40 L. Trotochaud, S. L. Young, J. K. Ranney and S. W. Boettcher, *J. Am. Chem. Soc.*, 2014, **136**, 6744–6753.

26790 | *J. Mater. Chem. A*, 2019, **7**, 26785–26790

This journal is © The Royal Society of Chemistry 2019